NASA/TM—2014-218418

Implementation of an Ultra-Bright Thermographic Phosphor for Gas Turbine Engine Temperature Measurements

Jeffrey I. Eldridge, Timothy J. Bencic, and Dongming Zhu
Glenn Research Center, Cleveland, Ohio

Michael D. Cuy
Vantage Partners, LLC, Brook Park, Ohio

Douglas E. Wolfe
Pennsylvania State University, University Park, Pennsylvania

Stephen W. Allison and David L. Beshears
Emerging Measurements, Knoxville, Tennessee

Thomas P. Jenkins
Metrolaser, Laguna Hills, California

Bauke Heeg
Lumium, Leeuwarden, The Netherlands

Robert P. Howard and Andrew Alexander
Aerospace Testing Alliance, Arnold Air Force Base, Tennessee

December 2014

NASA STI Program . . . in Profile

Since its founding, NASA has been dedicated to the advancement of aeronautics and space science. The NASA Scientific and Technical Information (STI) program plays a key part in helping NASA maintain this important role.

The NASA STI Program operates under the auspices of the Agency Chief Information Officer. It collects, organizes, provides for archiving, and disseminates NASA's STI. The NASA STI program provides access to the NASA Aeronautics and Space Database and its public interface, the NASA Technical Reports Server, thus providing one of the largest collections of aeronautical and space science STI in the world. Results are published in both non-NASA channels and by NASA in the NASA STI Report Series, which includes the following report types:

- TECHNICAL PUBLICATION. Reports of completed research or a major significant phase of research that present the results of NASA programs and include extensive data or theoretical analysis. Includes compilations of significant scientific and technical data and information deemed to be of continuing reference value. NASA counterpart of peer-reviewed formal professional papers but has less stringent limitations on manuscript length and extent of graphic presentations.

- TECHNICAL MEMORANDUM. Scientific and technical findings that are preliminary or of specialized interest, e.g., quick release reports, working papers, and bibliographies that contain minimal annotation. Does not contain extensive analysis.

- CONTRACTOR REPORT. Scientific and technical findings by NASA-sponsored contractors and grantees.

- CONFERENCE PUBLICATION. Collected papers from scientific and technical conferences, symposia, seminars, or other meetings sponsored or cosponsored by NASA.

- SPECIAL PUBLICATION. Scientific, technical, or historical information from NASA programs, projects, and missions, often concerned with subjects having substantial public interest.

- TECHNICAL TRANSLATION. English-language translations of foreign scientific and technical material pertinent to NASA's mission.

Specialized services also include organizing and publishing research results, distributing specialized research announcements and feeds, providing information desk and personal search support, and enabling data exchange services.

For more information about the NASA STI program, see the following:

- Access the NASA STI program home page at *http://www.sti.nasa.gov*

- E-mail your question to *help@sti.nasa.gov*

- Phone the NASA STI Information Desk at 757-864-9658

- Write to:
  NASA STI Information Desk
  Mail Stop 148
  NASA Langley Research Center
  Hampton, VA 23681-2199

NASA/TM—2014-218418

Implementation of an Ultra-Bright Thermographic Phosphor for Gas Turbine Engine Temperature Measurements

Jeffrey I. Eldridge, Timothy J. Bencic, and Dongming Zhu
Glenn Research Center, Cleveland, Ohio

Michael D. Cuy
Vantage Partners, LLC, Brook Park, Ohio

Douglas E. Wolfe
Pennsylvania State University, University Park, Pennsylvania

Stephen W. Allison and David L. Beshears
Emerging Measurements, Knoxville, Tennessee

Thomas P. Jenkins
Metrolaser, Laguna Hills, California

Bauke Heeg
Lumium, Leeuwarden, The Netherlands

Robert P. Howard and Andrew Alexander
Aerospace Testing Alliance, Arnold Air Force Base, Tennessee

National Aeronautics and
Space Administration

Glenn Research Center
Cleveland, Ohio 44135

December 2014

Acknowledgments

The authors thank the ARMD Seedling Fund for the opportunity to devote time and resources to develop a concept and bring it to engine testing maturity. We would also like to thank Harvey Niska of Honeywell for providing the stator vane doublet and Bill Stange of AFRL for allowing us to leverage testing opportunities provided by AFRL. Appreciation is also given to Matt Chambers, who made critical contributions to the discovery of the exceptional performance of Cr:GAP for phosphor thermometry.

Level of Review: This material has been technically reviewed by technical management.

Available from

NASA STI Information Desk
Mail Stop 148
NASA Langley Research Center
Hampton, VA 23681-2199

National Technical Information Service
5301 Shawnee Road
Alexandria, VA 22312

Available electronically at http://www.sti.nasa.gov

Implementation of an Ultra-Bright Thermographic Phosphor for Gas Turbine Engine Temperature Measurements

Jeffrey I. Eldridge, Timothy J. Bencic, and Dongming Zhu
National Aeronautics and Space Administration
Glenn Research Center
Cleveland, Ohio 44135

Michael D. Cuy
Vantage Partners, LLC
Brook Park, Ohio 44142

Douglas E. Wolfe
Pennsylvania State University
University Park, Pennsylvania 16802

Stephen W. Allison and David L. Beshears
Emerging Measurements
Knoxville, Tennessee 37922

Thomas P. Jenkins
Metrolaser
Laguna Hills, California 92653

Bauke Heeg
Lumium
Leeuwarden, The Netherlands

Robert P. Howard and Andrew Alexander
Aerospace Testing Alliance
Arnold Air Force Base, Tennessee 37389

Abstract

The overall goal of the Aeronautics Research Mission Directorate (ARMD) Seedling Phase II effort was to build on the promising temperature-sensing characteristics of the ultra-bright thermographic phosphor Cr-doped gadolinium aluminum perovskite (Cr:GAP) demonstrated in Phase I by transitioning towards an engine environment implementation. The strategy adopted was to take advantage of the unprecedented retention of ultra-bright luminescence from Cr:GAP at temperatures over 1000 °C to enable fast 2D temperature mapping of actual component surfaces as well as to utilize inexpensive low-power laser-diode excitation suitable for on-wing diagnostics. A special emphasis was placed on establishing Cr:GAP luminescence-based surface temperature mapping as a new tool for evaluating engine component surface cooling effectiveness.

Background

Luminescence-based temperature sensing has been shown to offer significant advantages over thermocouples and pyrometry for obtaining surface temperature measurements and offers measurement capability at combustion temperatures (Refs. 1 to 4). In particular, thermographic-phosphor-based temperature measurements have the potential for overcoming the attachment problem associated with thermocouples and the issues associated with unknown emissivity and interference by stray reflected radiation associated with pyrometry. Because of these advantages, thermographic-phosphor-based temperature measurements have been investigated for potential application in turbine engine environments (Refs. 1 to 11), particularly for engine components coated with thermal barrier coatings (TBCs) (Refs. 12 to 14). In the past, however, luminescence intensity at high temperatures has been insufficient for practical temperature measurements using thermographic phosphors in the highly radiant turbine engine environment. In particular, high-sensitivity, high-resolution surface temperature mapping using imaging techniques has been mostly limited to temperatures below 1000 °C (Refs. 8 to 11). Because of their lower emission intensity, surface temperature mapping using rare-earth doped phosphors usually requires applying the less temperature-sensitive peak intensity ratio method (Refs. 9 and 10). The higher emission intensity associated with transition-metal-doped phosphors allows the use of the more temperature-sensitive luminescence lifetime imaging approach. However, the lower thermal quenching temperatures associated with utilizing transition-metal-doped phosphors (Refs. 8 and 11) have until now restricted their application to temperatures below 1000 °C. The Phase I effort showed that the

extraordinary retention of ultra-bright luminescence intensity at temperatures above 1000 °C by Cr:GAP, several orders of magnitude more intense than state-of-the-art thermographic phosphors, presents an opportunity for the practical implementation of thermographic-phosphor-based temperature sensing that is uniquely well suited to the turbine engine environment (Refs. 15 and 16). The salient characteristic of the Cr:GAP phosphor that makes these measurements possible at turbine engine temperatures is the exceptionally high strength crystal field at the Cr^{3+} dopant site in the perovskite crystal structure, which results in a high energy barrier for non-radiative relaxation. This energy barrier suppresses thermal quenching until much higher temperatures compared with transition-metal-doped phosphors used in the past.

Transition metal dopants such as Cr are not normally considered for thermographic-phosphor-based temperature measurements above 1000 °C because of the aforementioned thermal quenching at lower temperatures. In addition, spin-allowed broadband luminescence emission by transition metal dopants is not usually suitable for thermographic phosphor measurements due to the extremely short radiative decay times and stronger thermal quenching than the spin-forbidden R-line emission. An explanation for the high-temperature persistence of spin-allowed broadband emission from Cr:GAP is given by Eldridge and Chambers (Ref. 15) and is summarized here. The primary mechanism (Ref. 17) is that in high-crystal-field Cr^{3+}-doped crystals, the long-lived ^2E energy level can act as a reservoir for the higher lying $^4T_2$ energy level that is responsible for the spin-allowed broadband emission via radiative relaxation to the $^4A_2$ ground state. Figure 1 shows a single configurational coordinate diagram for high-crystal-field (where the $^4T_2$ level is higher in energy than the ^2E level) Cr^{3+}-doped crystals such as Cr:Al_2O_3 and Cr:GAP, where ΔE is the energy difference between the $^4T_2$ and underlying ^2E levels, ΔE_q is the energy barrier between the zero-phonon $^4T_2$ state to the $^4T_2$-to-$^4A_2$ crossover by multiphonon absorption, and Δ_{FC} is the Franck-Condon offset between the $^4T_2$ and $^4A_2$ parabolas. At increasing temperatures, thermal equilibrium between the ^2E and $^4T_2$ levels results in an increasing promotion of ions from the much longer-lived ^2E reservoir level to the $^4T_2$ level. Therefore, the spin-allowed broadband radiative emission associated with the relaxation from the $^4T_2$ to $^4A_2$ ground state increases as the emission associated with the spin-forbidden ^2E to $^4A_2$ radiative transition decreases. At even higher temperatures, non-radiative crossover from the $^4T_2$ to $^4A_2$ states increases because of the increasingly populated phonon energy levels and leads to the eventual thermal quenching of the spin-allowed broadband emission. Because thermal equilibrium is maintained between the ^2E and $^4T_2$ populations, the observed decay time of the observed ^2E to $^4A_2$ emission, τ_{2E}, and that of the $^4T_2$ to $^4A_2$ broadband emission, τ_{4T2}, both reflect the depopulation of the ^2E reservoir. Therefore, $\tau_{2E} = \tau_{4T2}$. Zhang et al. (Ref. 17) showed that the decay time associated with these ^2E reservoir depopulation processes as a function of temperature, T, can be expressed by:

$$\tau_{4T2} = \tau_{2E} = \tau_{2E}^{R} \frac{1 + 3e^{-\Delta E / kT}}{1 + \alpha e^{-\Delta E / kT} + \beta e^{-(\Delta E_q + \Delta E)/kT}} \qquad (1)$$

where $1/\tau_{2E}^{R}$ is the intrinsic radiative rate of the ^2E to $^4A_2$ transition, $\alpha = \tau_{2E}^{R}/\tau_{4T2}^{R}$, $\beta = \tau_{2E}^{R}/\tau_q$, $1/\tau_{4T2}^{R}$ is the intrinsic radiative rate of the $^4T_2$ to $^4A_2$ transition, $1/\tau_q$ is a scaling factor for the non-radiative $^4T_2$ to $^4A_2$ crossover rate, and k is Boltzmann's constant. Assuming α and β » 1, this relationship shows that thermal quenching of the observed broadband $^4T_2$ to $^4A_2$ transition can be delayed to higher temperatures by increases in ΔE and in ΔE_q. The Tanabe-Sugano diagram for $3d^3$ electron configurations (Fig. 2) indicates that ΔE increases with the strength of the crystal field. Furthermore, ΔE_q increases with stronger bonding, because the stronger restoring force on a displaced ion will result in a greater steepening of the $^4T_2$ parabola (involves bonding orbitals) than the $^4A_2$ parabola (does not involve bonding orbitals).

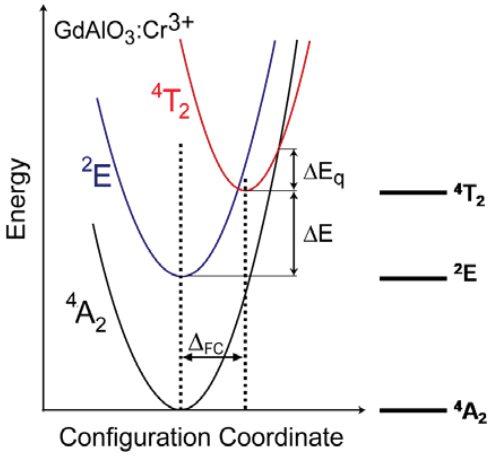

Figure 1.—Single configurational coordinate plot (left) and energy level diagram (right) for high-crystal-field Cr^{3+}-doped phosphors such as Cr:GAP.

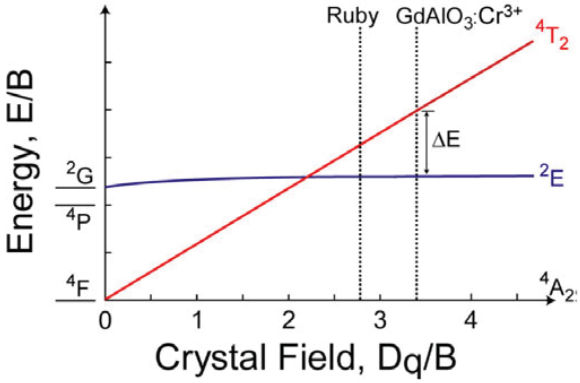

Figure 2.—Tanabe-Sugano diagram showing relationship between $^4T_2$ and ^2E energy levels and crystal field for Cr^{3+} $3d^3$ electron configuration. Dotted lines show that higher crystal field in Cr:GAP will lead to substantially higher energy difference between these levels compared to ruby.

In view of these considerations, rare-earth (RE) aluminate orthorhombic perovskites, $REAlO_3$, are ideal crystal hosts for Cr^{3+} dopants. The Cr^{3+} dopant ions substitute for the Al^{3+} ions in the tightly bound AlO_6 octahedra within the $REAlO_3$ perovskite structure, resulting in exceptionally strong crystal fields (20 percent higher at Al^{3+} sites in $GdAlO_3$ compared with Al_2O_3) and therefore a substantially greater ΔE as shown in Figure 2. Among the rare-earth aluminate perovskites, $REAlO_3$, only the perovskites with RE = Gd, Tb, Dy, Y, Ho, Er, and Tm retain an orthorhombic perovskite structure from room temperature to above 1000 °C. The others exist in either rhombohedral or cubic structures, with undistorted cubic symmetry at the Al^{3+} sites in the AlO_6 octahedra, and therefore will exhibit undesirably weak excitation transition oscillator strengths. Among the remaining candidate rare-earths, the crystal field at the Al^{3+} octahedral sites is expected to decrease in the order from largest to smallest ionic radii (Gd>Tb>Dy>Y>Ho>Er>Tm). Therefore, Cr:GAP is expected to delay thermal quenching of the spin-allowed broadband emission to higher temperatures than the other perovskite candidates.

Figure 3 shows the luminescence emission spectra of a Cr:GAP specimen as a function of temperature. It is evident from these spectra that the spin-allowed broadband emission centered at 640 nm becomes more prominent while the spin-forbidden R-line emission at 728 nm along with its vibrational side bands become less prominent with increasing temperature. It is also apparent that at the highest temperatures (>700 °C), the shorter-wavelength broadband emission dominates the emission spectra and therefore is the only component of luminescence emission remaining that can be used for temperature measurements. While the peak of broadband emission is at about 640 nm, a bandpass filter centered at

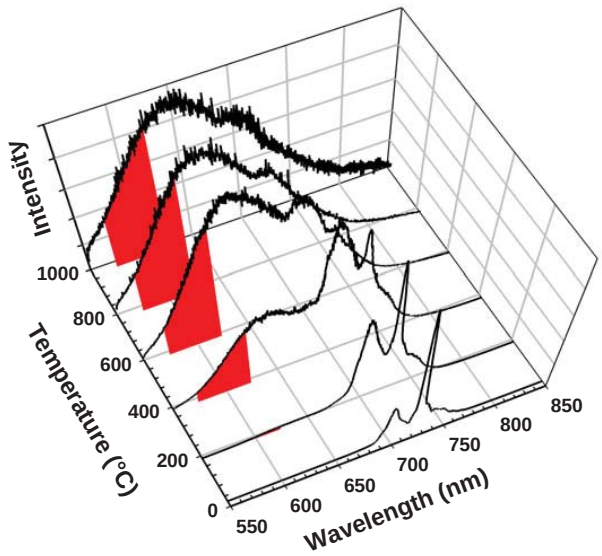

Figure 3.—Temperature dependence of luminescence emission spectra for Cr:GAP. Excitation at 532 nm. Red-shaded regions show wavelength range corresponding to bandpass selected for luminescence decay measurements.

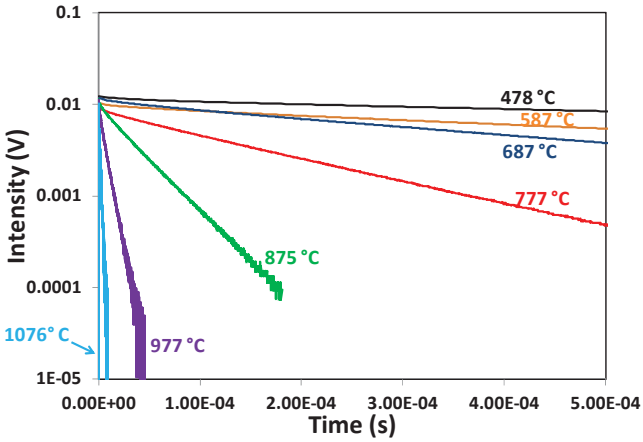

Figure 4.—Luminescence decay at various temperatures from Cr:GAP, using bandpass filter centered at 590 nm with a full-width half-max of 40 nm.

590 nm with a full-width at half-maximum of 40 nm was chosen to select the wavelength range detected by the photomultiplier tube (PMT) used to acquire the luminescence decay curves. This choice was made as a compromise between emission intensity and the benefit of shifting to shorter wavelengths where there is lower thermal radiation background.

The temperature dependence of Cr:GAP luminescence decay curves acquired at various temperatures up to 1076 °C is shown in Figure 4. Although these decay curves are nearly single exponential, a double exponential equation was fitted to the data to take into account a short, fast initial decay: $I = I_1 e^{-t/\tau_1} + I_2 e^{-t/\tau_2}$, where I is the intensity, t is time, τ_1 is the time constant associated with the short initial decay, and τ_2 is the time constant associated with the dominant long-term decay. The values of τ_2 were used for temperature calibration.

Based on the determined decay constants, the relationship between decay time, $\tau = \tau_2$, and temperature up to 1075 °C is shown in Figure 5. The solid line in Figure 5 is the fit of a model (Ref. 15) to the data. Figure 5 shows that Cr:GAP decay time exhibits maximum temperature sensitivity (steeper slope) above 700 °C. This calibration then allows determining an unknown temperature, T, from a decay time, τ, in Equation (1) by an iterative solution of the inverse problem.

This high-temperature retention of ultra-bright luminescence intensity with highly temperature-sensitive decay time was exploited in Phase II to meet several enabling test capability objectives. The first goal was to overcome the usually intensity-starved nature associated with non-intrusive probing of the engine environment. Probes designed for engine insertion are constrained to provide much more limited laser excitation intensity and solid angle of detection than typical laboratory setups. Therefore, a major goal of the Phase II effort was to demonstrate successful temperature monitoring using a probe designed for engine insertion. The second major goal was to transition from spot temperature measurements to 2D temperature mapping by simply broadening the excitation laser beam to cover the region of interest. This has not been

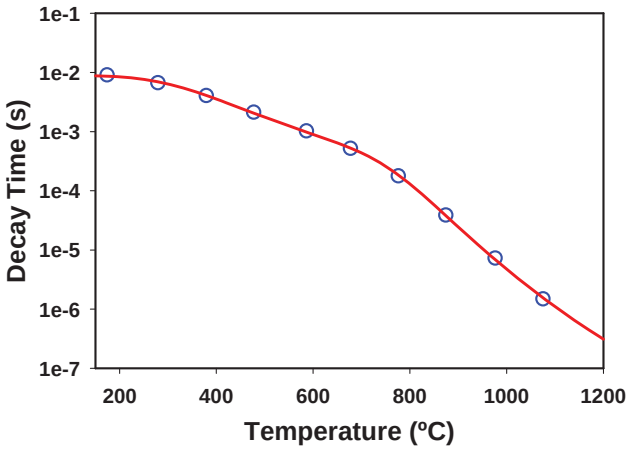

Figure 5.—Temperature dependence of Cr:GAP luminescence decay time for wavelengths selected by bandpass filter centered at 590 nm with a full-width half-max of 40 nm. Circles are values determined from measurements. Solid line is obtained by fitting Equation (1) to the data.

previously practical because expansion of laser beam reduced signal to noise to unacceptable levels. The focus of the temperature mapping effort was to evaluate thermal gradients surrounding cooling holes under conditions approaching the turbine engine environment. The establishment of this 2D temperature mapping approach that is not dependent on surface emissivity and insensitive to reflection of background thermal radiation will be an enabling tool for evaluating performance of engine component cooling strategies in a turbine engine environment. The third goal was to take advantage of the ultra-bright luminescence to demonstrate on-wing-compatible temperature measurements to 1000 °C using low-powered LED or laser diode excitation integrated into an engine probe.

Approach

Demonstration of spot temperature measurements using a light delivery and detection constrained probe designed for engine insertion was accomplished by leveraging an opportunity provided by the Air Force Versatile Affordable Advanced Turbine Engines (VAATE) project that had expressed interest in testing the Cr:GAP thermographic phosphor that had been developed in the Seedling Phase I effort. This was a mutually beneficial opportunity: the Air Force was able to include a phosphor with superior performance compared with those previously considered, and the Seedling project would in turn have access to a VAATE-designed probe designed for engine insertion, a Honeywell stator vane doublet for coating, and a piggyback test opportunity at the J85 engine test facility at University of Tennessee Space Institute (UTSI), operated by Arnold Engineering Development Center (AEDC).

A multi-stage effort was also followed that proceeded towards the ultimate goal of 2D temperature mapping of the area surrounding cooling holes in a commercial high-pressure turbine vane exposed to an engine combustion environment. Initial demonstrations were performed evaluating thermal test patterns produced on 25.4-mm diameter superalloy disks that were coated with a 7YSZ TBC and a Cr:GAP surface layer by electron-beam physical vapor deposition (EB-PVD). These experiments were performed to demonstrate the temperature sensitivity and spatial resolution possible for 2D temperature mapping. These sensitivity experiments were followed by more engine-relevant temperature mapping, which included cooling air jet impingement on button specimens, and then advanced to Cr:GAP-coated stator vane doublet with air film cooling in both NASA burner rig tests as well as UTSI J85 afterburner tests. The thermal test patterns were produced using a “fly-eye” lens to produce a thermal “test pattern” via CO_2 laser heating. This approach provides an excellent test of the spatial resolution achieved in the 2D temperature maps. Optimization of gated image timing parameters and engine processing was performed using the laser heating facility before burner rig and combustion environment testing was attempted. Procedures for accurate background subtraction and gate delay selection were investigated. The next step was to perform the optimized time-gated imaging on a stator vane in an actual flame environment provided by the NASA burner rig facility. The final demonstration was in the combustion environment provided by the more realistic broad, uniform heat-flux afterburner flame of a J85 test engine at UTSI.

Low-power laser diode excitation that is compatible with on-wing diagnostics was demonstrated by integrating the laser diode excitation with the same VAATE-designed optical probe previously developed for insertion into a Honeywell TECH7000 engine. Testing was coordinated with the 2D temperature mapping effort for efficient progress.

Research Results

Engine Probe Spot Temperature Measurements

An opportunity arose in early fall 2012 to piggyback onto an Air Force VAATE test at UTSI. A stator vane doublet was provided by Honeywell, onto which a Cr:GAP coating was deposited. The vane was coated at Penn State by EB-PVD where vane rotation fixturing was developed to produce a uniform coating on this complex shape. The coated vane in the test fixture is shown in Figure 6. The VAATE-designed engine probe was located below the hole in the vane sidewall seen in Figure 6. The probe contained a bifurcated fiber optic bundle with a central excitation fiber that splits off for coupling with a pulsed 532 nm laser (New Wave Polaris III) and surrounding collection fibers that split off and are routed for detection by a PMT after transmission through a bandpass filter centered at 590 nm with a full-width half-max of 40 nm.

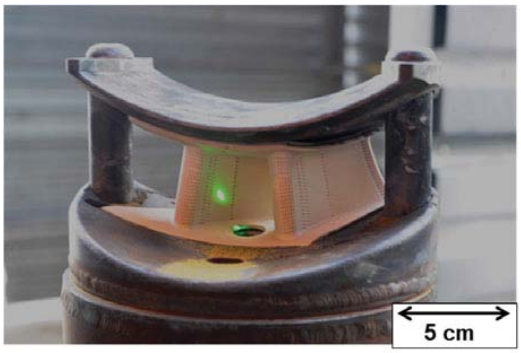

Figure 6.—Honeywell stator vane in AEDC test fixture. Green spot is excitation laser showing location of temperature measurement.

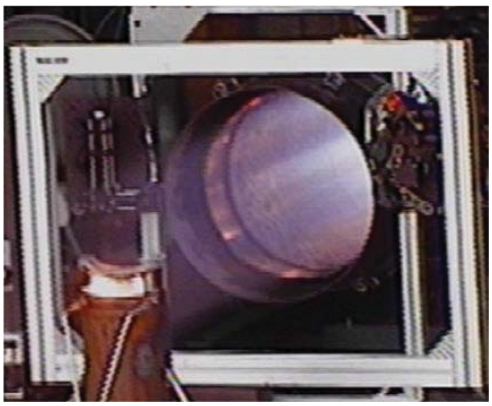

Figure 7.—Aft view of Cr:GAP-coated Honeywell stator vane doublet in afterburner flame of J85 test engine at UTSI.

Figure 8.—Front view of Cr:GAP-coated Honeywell stator vane doublet in afterburner flame of J85 test engine at UTSI.

Figure 7 shows the vane mounted in the afterburner flame of the J85 test engine, and Figure 8 shows a front view of the vane as it was being heated in the afterburner flame. The green spot on the pressure side of the left-hand vane is the laser excitation spot and therefore indicates the location of the temperature measurements.

Spot temperature measurements were obtained by measuring luminescence decay times and then converting decay time to temperature via calibration curves. Figure 9 shows a semilog plot of PMT signal (or emission intensity) decay at different afterburner power settings. These decays were then fitted by a bi-exponential, with a short and long decay time, and the long decay time was then used for temperature indication. This decay time was converted to temperature by using decay time/temperature calibration data which could be fitted by Equation (1) to provide the relationship between decay time and temperature indicated by the blue curve in Figure 10. A temperature value can then be assigned to each decay time based on where it lies on the calibration curve. Reproducible spot temperature measurements were obtained at a variety of afterburner throttle settings (PLA = power lever angle), with results from two throttle level sequences shown in Figure 10. These power level settings resulted in measured surface temperatures that spanned a range from 550 to 1027 °C.

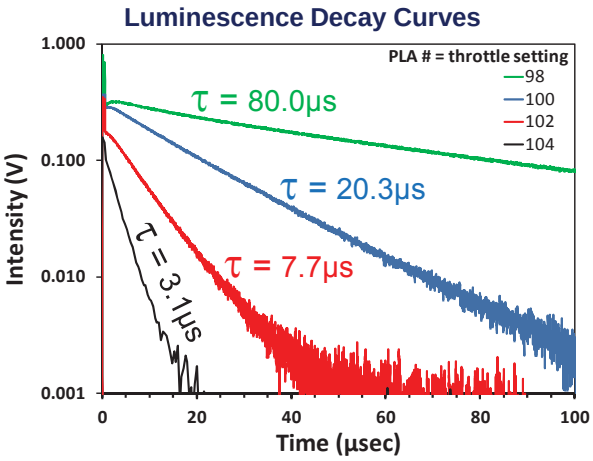

Figure 9.—Luminescence decay curves acquired from Cr:GAP-coated vane at different throttle settings of J85 test engine at UTSI.

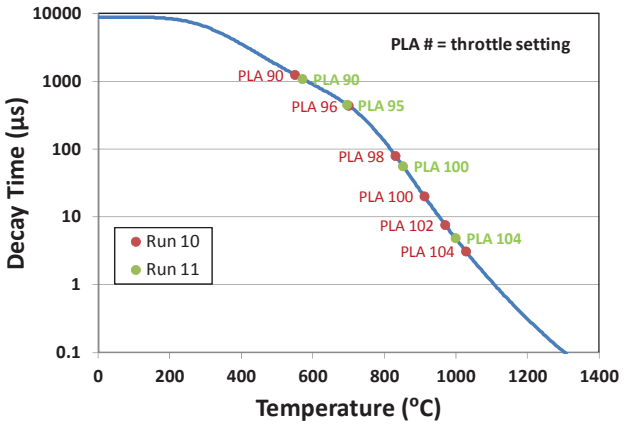

Figure 10.—Temperatures determined from luminescence decay time for Cr:GAP-coated vane at different throttle settings of J85 test engine at UTSI. Blue curve shows calibration between decay time and temperature.

In terms of signal to noise, the Cr:GAP phosphor greatly outperformed the other candidate phosphors that were being downselected for future testing by the Air Force. The other phosphors tested included Dy:YAG, Tm:YAG, and Eu:YSZ; all showed substantially lower high temperature luminescence emission intensity compared with Cr:GAP. On the basis of these impressive results, the Air Force decided to adopt Cr:GAP as one of two thermographic phosphors for subsequent testing at Honeywell as part of the VAATE program.

2D Temperature Mapping

Thermal Test Patterns

2D temperature mapping by time-gated imaging using an intensified CCD (ICCD) camera was first performed on Cr:GAP-coated specimens heated in the NASA Glenn high heat flux laser facility. Beam expansion optics were configured so that the normally focused pulsed 532 nm laser spot was expanded to illuminate the entire 25.4-mm diameter specimen. The specimen was subjected to a high heat flux by a combination of high power CO_2 laser surface heating and backside forced air cooling. Calibration data were obtained by collecting gated images for specimens heated to a sequence of uniform surface temperatures from 800 to 1250 °C. The ICCD (PI-MAX4, Princeton Instruments) was aligned to be focused on the specimen surface. Although the camera's 16-bit analog to digital converter provides a maximum of 65535 counts/pixel (which matches the 130000 electron well capacity of the CCD), acquisition was restricted to 10000 counts/pixel (unbinned) because it was important to stay in the linear response range of the ICCD. Lindén et al. (Ref. 18) have shown that intensifier response becomes noticeably nonlinear well before 50 percent of CCD well capacity. An 8-μm pyrometer was aimed at the center of the specimen to provide a pyrometer-based temperature measurement for comparison. The laser Q-switch output pulse was used to synchronize collection of images by the ICCD at the desired delay times after the laser pulse. Time-gated images are collected over a sequence of delay times after the laser pulse, and from this stack of images, a decay time can be determined at each pixel. To produce the image stack, after each laser pulse, an image is collected at a selected delay time after the laser pulse with exposure with a selected duration. If signal to noise is insufficient for the selected exposure time, then multiple exposures at the same delay time will be averaged on-chip before stepping to the next delay time in the sequence. The first demonstration of 2D temperature gradient mapping was performed by laser heating through a stationary 81-element "fly-eye" ZnSe lens that produces a distinct thermal pattern on the specimen surface, essentially producing a thermal "test pattern." In normal operation the "fly-eye" lens is used to generate uniform heating over the specimen surface. Because the multi-element lens design produces a diffraction pattern that results in hot spots, the "fly-eye" lens is normally rotated to homogenize the heating profile. For this application, however, the "fly-eye" lens was not rotated and the thermal test pattern is the result of the diffraction pattern produced by transmission of the CO_2 laser beam through the 81-element "fly-eye" lens.

Producing 2D thermal maps from a sequence of time-gated images is a multi-step process. As shown in Figure 11(a), even without any laser excitation of luminescence, there is significant nonuniform thermal radiation from the specimen, where the hotter bright spots are produced by nonuniform CO_2 laser heating. An image acquired 16 μs after the laser excitation pulse (Fig. 11(b)) shows a superposition of both the excited luminescence emission and thermal background intensity. Because of shadowing effects, there is a crescent-shaped section on the left side of Figure 11(b) where there was no laser excitation and which therefore shows background radiation but no luminescence. In the much larger area of overlap between luminescence and background radiation intensity, there is an obvious need to subtract the non-negligible background contribution. Therefore, an image collection procedure was implemented where collection of background images (with no laser excitation) was regularly interspersed with the collection of luminescence image sequences. The success of this approach is observed in Figure 11(c), where the background has been effectively removed from Figure 11(b). It should be noted that the intensity in the background-corrected luminescence image (Fig. 11(c)) has an inverse relationship to the intensity in the background radiation image (Fig. 11(a)). This inverse relationship occurs because hotter regions (which are brighter in the background image) lose luminescence intensity more quickly than cooler regions due to the faster luminescence decay times at higher temperature.

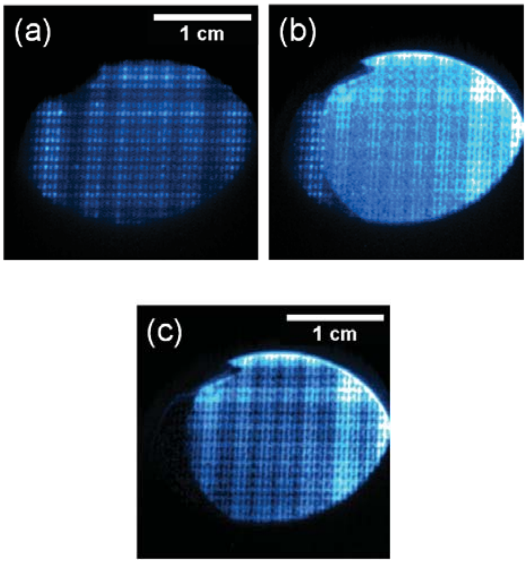

Figure 11.—Background subtraction for luminescence images of thermal "test pattern" produced by CO_2 laser heating of surface of Cr:GAP-coated disk. (a) Background image with no laser excitation. (b) Luminescence image obtained 16 μs after laser pulse without background subtraction. (c) Same luminescence image after background subtraction.

Incorporating this background subtraction procedure, 2D temperature maps could be produced from a set of background-corrected luminescence images collected over a sequence of gate delays (time between laser pulse and image collection). A stack of images was collected where each image in the stack corresponded to a different gate delay. Therefore, at each pixel in the stack, a luminescence decay curve could be constructed, fitted to determine a decay time, and then converted to temperature by a decay time to temperature calibration. As an example, Figures 12(a) and (b) show background-corrected luminescence images collected 0.5 and 5.0 μs after the laser pulse, respectively. Note that greater contrast occurs in the longer gate delay image (Fig. 12(b)) because luminescence from the hotter regions has decayed much faster than the cooler regions. A decay time map (Fig. 12(c)) was produced by fitting to the decay curve constructed at each pixel from the background-corrected multi-image stack (in this example, a 20-image stack). A single exponential fit to the decay curve associated with each pixel was performed using the program PixBleach (Ref. 19), which is a plug-in module for ImageJ, a public domain, Java-based image processing program developed at the National Institutes of Health. Because a background correction had already been made, no offset term was included in the fit to the single exponential. The resultant decay time map (Fig. 12(c)) shows a decay time range of about 2 to 10 μs, with shorter decay times (darker) corresponding to hotter regions. Calibration curves were then utilized to convert the decay time map (Fig. 12(c)) to a temperature map (Fig. 12(d)). While conversion of decay time to temperature was performed by an iterative inverse solution of Equation (1) for spot temperature measurements, this procedure was too time-consuming for 2D temperature mapping. For example, a high resolution 1024×1024 image stack would require fitting over 1×10^6 decay curves, and a lower resolution 256×256 image stack would still require fitting over 6.5×10^4 decay curves. Therefore, for 2D temperature mapping, a simplification was made based on the fact that there is close to a linear relationship observed in Figure 5 between the log of decay time and temperature. Using this simplification, conversion of decay time to temperature could be performed much more rapidly for the 2D temperature maps using the relationship determined by linear regression over the temperature range from 850 to 1250 °C:

$$T = -74.1\ln(\tau) + 1127.3 \qquad (2)$$

where T is temperature in °C and τ is decay time in μs. The resulting 2D temperature map (Fig. 12(d)) shows temperatures in the field of view range from approximately 950 to 1050 °C. A temperature line scan (location indicated by yellow line in Figure 12(d)) is shown in Figure 12(e), and provides a more quantitative indication of the periodic temperature variation across the thermal "test pattern."

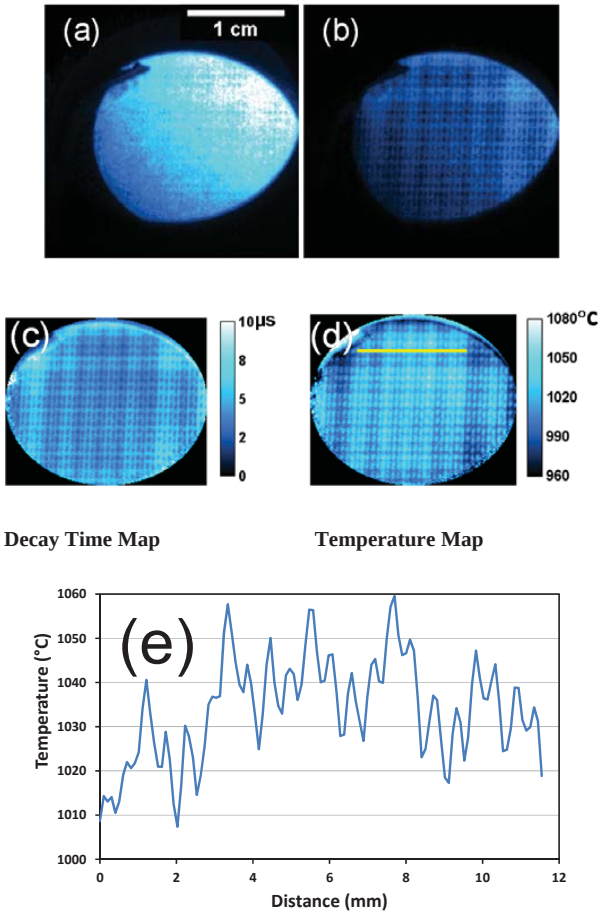

Figure 12.—2D temperature map construction for thermal "test pattern." Background-corrected luminescence images obtained 0.5 μs (a) and 5.0 μs (b) after laser pulse. (c) Luminescence decay time map. (d) 2D temperature map. (e) Temperature line scan corresponding to yellow line in (d).

Using this procedure, 2D temperature maps (Figs. 13 to 15) were produced that showed how the thermal test pattern changes with increasing applied heat flux (heat fluxes #1-3 in increasing order). These figures show that the diffraction hot spots can be resolved even at temperatures above 1200 °C, although there is some spatial smearing at the highest temperatures. However, at least in the 1000 to 1100 °C range, impressive temperature sensitivity and spatial resolution is observed, with an ability to detect temperature changes of 5 °C over sub-millimeter distances. It is important to note that unlike pyrometry, these temperature maps are insensitive to surface emissivity and reflected radiation.

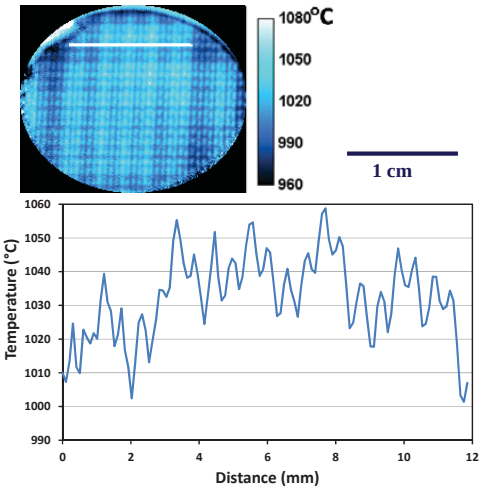

Figure 13.—(top) 2D temperature map of thermal test pattern at heat flux #1. Map produced from 20-gate-delay sequence, 10 repeats for each gate delay, gate delay increment = gate width = 0.5 μs. (bottom) Temperature line scan corresponding to white line.

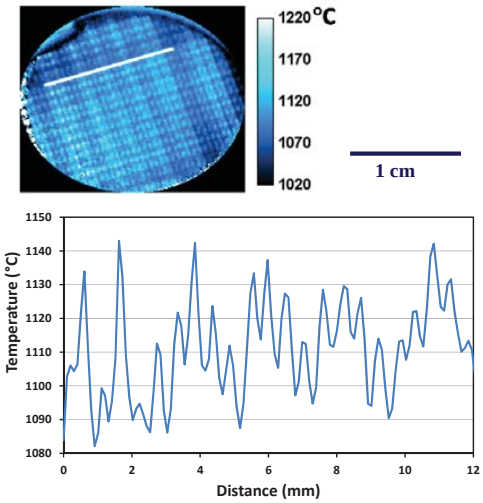

Figure 14.—(top) 2D temperature map of thermal test pattern at heat flux #2. Map produced from 20-gate-delay sequence, 10 repeats for each gate delay, gate delay increment = gate width = 0.5 μs. (bottom) Temperature line scan corresponding to white line.

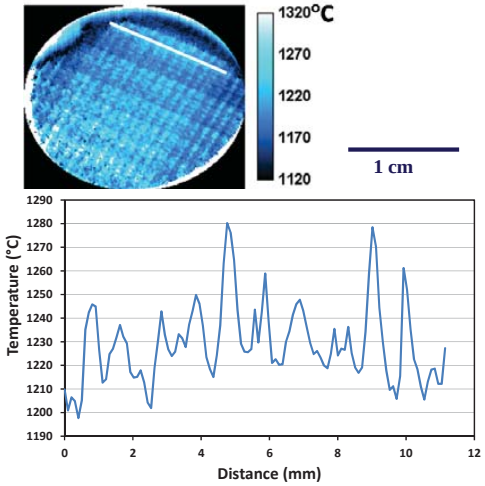

Figure 15.—(top) 2D temperature map of thermal test pattern at heat flux #3. Map produced from 20-gate-delay sequence, 10 repeats for each gate delay, gate delay increment = gate width = 0.1 μs. (bottom) Temperature line scan corresponding to white line.

Dual Gate Acquisition for Faster Temperature Sampling

All of the 2D temperature maps were obtained by multiple gate delay acquisition (typically, a sequence of 20 gate delays) for highest accuracy. This approach, however, is restricted to quasistatic thermal conditions as images are collected over a sequence of delay times. Therefore, for transient thermal conditions, it would be desirable to trade off accuracy for speed (possibly approaching video rates). Because of this motivation for fast data acquisition, the prospect of producing 2D temperature maps from only two gate delays was investigated. The primary issue with limiting to dual gate delay acquisition is that decay time determination can be very sensitive to the selection of the gate delay times. At any given pixel, if either gate delay resides in the early fast decay or in the noise at long decay, significant temperature errors can occur.

Guidance for dual gate selection was provided by first applying dual gate delay selection to simulated luminescence decay curves to determine the effect of gate selection on single decay τ estimates from idealized biexponential decays. The simulated data was based on a biexponential, $I = I_1 e^{-t/\tau_1} + I_2 e^{-t/\tau_2}$, with $\tau_1 = 20$ μs and $\tau_2 = 120$ μs. The first of the two gate delays was held fixed at $\tau = 0$ μs and the second gate delay, Δt, was varied. Figure 16(a) shows that the estimated τ increases and approaches an asymptotic plateau value as Δt increases. This is expected because the influence of the initial fast decay is reduced the further out the second gate delay is selected. Note that the τ estimate gets close but never quite reaches $\tau_2 = 120$ μs. While Figure 16(a) makes a good case for choosing the second gate delay at as long a time as possible, the disadvantage is that the emission intensity will become vanishingly small at long times and susceptible to background noise. To address this issue, background noise was added to the simulated decay and the analysis of the effects of gate selection on τ estimate was repeated with results shown in Figure 16(b). This figure shows the disadvantage of selecting the second gate delay into regions with very low signal to noise as this biases the estimated τ towards increasingly greater values. Therefore, there is a compromise range for Δt selection—in this case a plateau between about 150 and 350 μs—where the τ estimate is relatively insensitive to the selection of Δt. This relative insensitivity arises where Δt is long enough to not be strongly affected by the initial decay τ_1, while not being biased by background noise. This behavior also gives added advantage to acquiring higher signal-to-noise data because that will extend the plateau region to longer Δt values. Therefore, it may be beneficial to make the second gate width longer than the first gate width.

The analysis of the effect of dual gate delay selection was then applied to actual data. Time-gated luminescence images were collected for a uniformly heated specimen over a wide range of narrowly spaced decay times. Decay times were determined from a systematic selection of dual gate delay time pairs. Each curve in Figure 17 represents decay times determined by the selection of a particular initial gate delay, with each point in that curve representing a choice of the second gate delay for a specimen laser-heated to a uniform surface temperature of 1250 °C. It is clear that if the initial gate delay is selected too early (lower curves) or too late (upper curves) a plateau decay time, τ_{est}, is not obtained. In all cases, the τ_{est} values increase continuously once the second gate delay selection moves into the background noise, as predicted by the simulations. Fortunately, with initial gate delay selection at intermediate values (curves 3–10), a plateau region occurs where τ_{est} is insensitive to selection of the second delay gate (intra-frame delay). Using curve 5 (initial gate delay = 85 ns) as an example, there is a stable plateau region for selection of the second gate delay (from about 50 to 200 ns) where a stable decay time of about 150 ns is obtained. Therefore, even at the upper temperature limit of 1250 °C, where signal to noise is relatively poor, a dual gate selection can be made that produces a robust decay time determination, albeit over only a modest range of gate delay intervals.

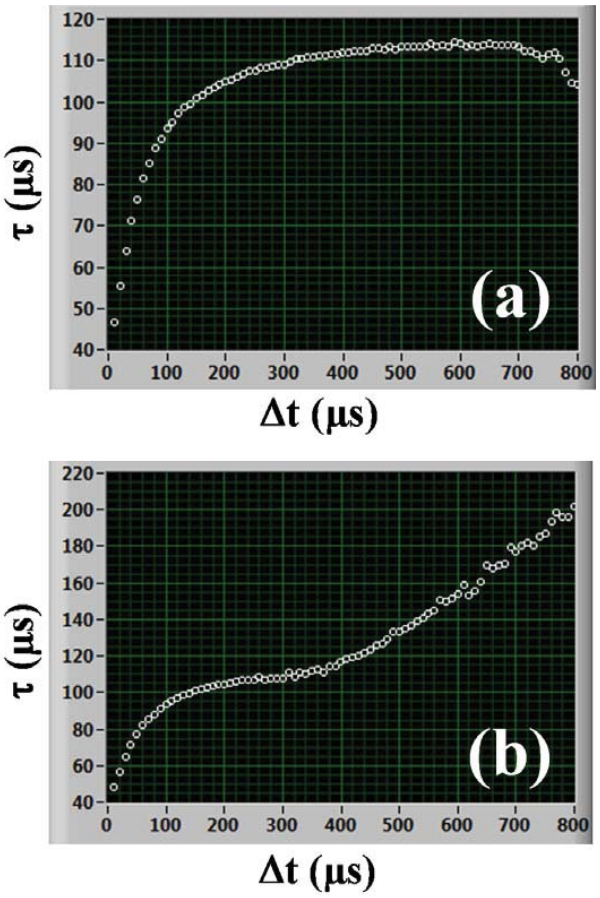

Figure 16.—Effect of dual gate selection on estimated single decay constant, τ, obtained from simulated biexponential decay with $\tau_1 = 20$ μs and $\tau_2 = 120$ μs. Initial gate delay is fixed at start of decay and Δt is time interval between first gate delay and second gate delay. (a) No background noise included in simulation. (b) Background noise included in simulation.

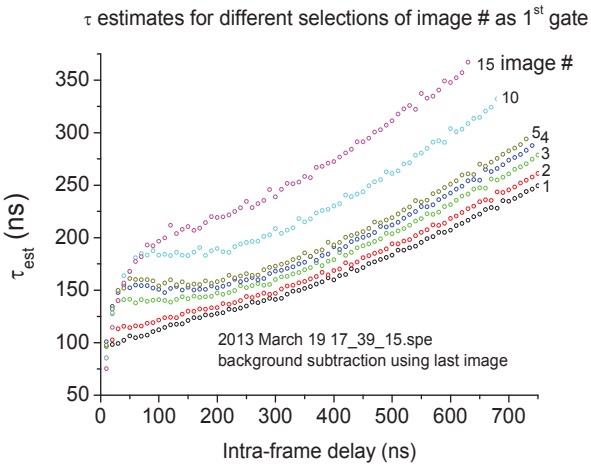

Figure 17.—Estimates of decay time, τ_{est}, determined from different dual gate delay selection times from luminescence images of a 25.4 mm diameter specimen heated by CO_2 laser to uniform temperature of 1250 °C. Each curve represents selection of specific initial gate delay time with each point in the curve representing choice of the second gate delay time. Each curve number increment corresponds to selecting the initial gate delay 10 ns later than the previous curve number, starting with an initial gate delay of 45 ns for curve 1.

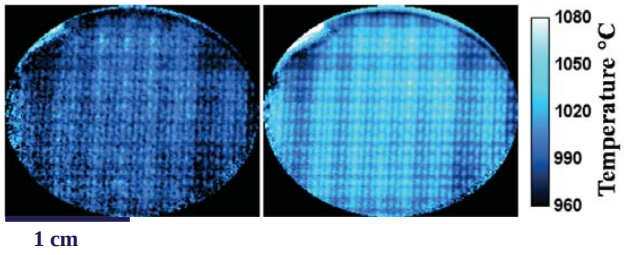

Figure 18.—The 2D temperature maps of thermal test pattern observed in Figure 13 obtained by (a) dual gate (2 and 5 μs gate delays) and multigate (20) decay time determination.

An appropriate dual-gate selection was then performed (using gate delays at 2 and 5 μs) to produce the 2D temperature map of the thermal test pattern previously shown in Figure 13 (ignoring the remaining 18 gate delays). Figure 18 shows a side-by-side comparison of the 2D temperature maps obtained by both the dual and previous multigate selection. While it is apparent that there is much more scatter along with an offset to lower temperature in the dual-gate temperature map (Fig. 18(a)), this may be a justifiable sacrifice if the 10 times increase in effective temperature sampling speed is needed to monitor changing temperatures.

Cooling Air Jet Impingement

One of the original goals of the Phase II effort was to demonstrate 2D temperature maps around the vicinity of cooling holes. However, even with forced air cooling through cooling holes laser-drilled through button specimens, negligible localized cooling was observed in the vicinity of the holes for laser-heated specimens. After consultation with NASA experts in air film cooling, it was realized that the air jets exiting the cooling holes will produce surface cooling only in the presence of a strong cross flow (as is present in a turbine engine) that pushes down the air jet to the specimen surface. Because of this realization, an alternative approach was adopted, which was to direct cooling air jets across the surface of the specimen from small diameter nozzles positioned above the specimen surface, as shown in Figure 19.

In the same manner as for the thermal "test pattern," a 2D temperature map for cooling air jet impingement was produced for average temperatures up to 1200 °C, and an example is shown in Figure 20 of the thermal distribution produced by the cooling air jets for an average surface temperature of 1000 °C. From the 2D temperature map, it is apparent that there was greater air flow from the two nozzles on the left-hand side than the two on the right-hand side. It is important to note that, unlike pyrometry, this thermal map has the advantage of being insensitive to surface emissivity and reflected radiation.

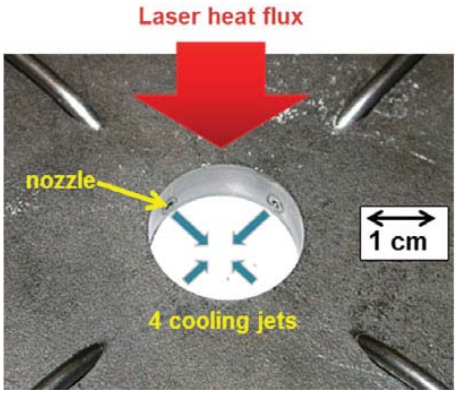

Figure 19.—Cooling air jet fixture for high heat flux laser heating facility.

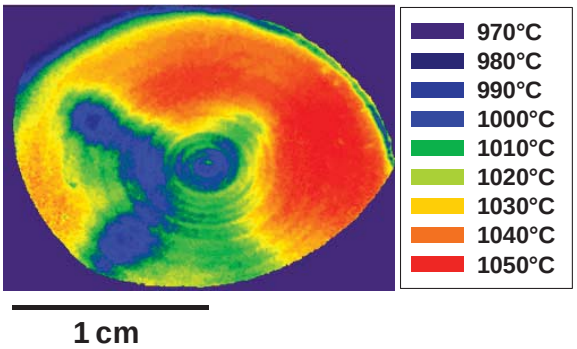

Figure 20.—The 2D temperature map of laser-heated Cr:GAP-coated disk subjected to crossed cooling air jets. Map produced from 8-gate-delay sequence, 10 repeats for each gate delay, gate delay increment = gate width = 3.0 μs.

Surface Temperature Measurements of Vane in Burner Rig Flame

The successful development of procedures and analysis for obtaining 2D temperature mapping of 25.4-mm diameter specimens subjected to well controlled heat flux conditions was followed by extension to the more relevant demonstration of surface temperature mapping of a Cr:GAP-coated Honeywell stator vane doublet during testing in the NASA GRC Mach 0.3 burner rig facility. The Cr:GAP phosphor had been adopted for an Air Force Research Laboratory (AFRL)-funded VAATE engine test at UTSI in September 2012 and the Cr:GAP-coated Honeywell stator vane doublet was made available for the NASA Seedling effort after the UTSI engine test was completed. Fixturing was developed for the NASA burner rig so that adjustable cooling air flow could be supplied to pass through the cooling holes in the vane during exposure to the burner rig flame (Fig. 21(a)). The pulsed 532 nm excitation laser passed through a 10x beam expander and was positioned to illuminate the area of interest with diameter approximately 5 cm (Fig. 21(b)). The ICCD was aligned to be focused on the region illuminated by the excitation laser. The laser Q-switch output pulse was used to synchronize collection of images by the ICCD at the desired delay times after the laser pulse. An 8-μm pyrometer was also aimed just downstream of the leading edge to provide a pyrometer-based temperature measurement for comparison. Figure 21(c) shows a photograph of the stator vane doublet as it is heated in the burner rig flame. Using the same procedures as were developed for the 25.4-mm diameter specimens in the high heat flux laser facility, background-corrected luminescence images over a sequence of up to 64 gate delay times were collected for different combinations of burner flame setting and cooling air flows. Figures 22 to 24 show surface temperature maps obtained at low, medium, and high burner flame settings, respectively. At each burner flame setting, surface temperature maps were acquired for three levels of cooling air flow through the vane cooling holes. These three levels of cooling air flow were maintained by setting the pressure of the cooling air input manifold to 0, 10, or 20 psi. The effect of cooling air flow is observed most clearly at the highest cooling flow condition (Figs. 22(c), 23(c), and 24(c)) where there is a clear effect of both overall vane temperature reduction as well as a distinct cool zone just downstream of the leading edge showerhead cooling holes. Presumably, the overall temperature reduction is due primarily to internal cooling air impingement, whereas the cool zone just downstream of the leading edge cooling holes is more likely produced by air film cooling. In addition, there is an obviously greater reach of cooling from the cooled side walls. Visible light photographs for each burner flame/cooling flow condition are shown in Figures 22 to 24. Note that the pattern of the visible thermal radiation qualitatively matches the temperature map pattern. Line scans across the temperature maps (Fig. 25) give a better quantitative indication of the noise level and the effect of cooling air flow. Figure 25(a) shows the downstream-to-upstream location of all the line scans, which are shown for low flame (Fig. 25(b)), medium flame (Fig. 25(c)), and high flame (Fig. 25(d)) settings with the same three cooling air flow conditions for each flame setting. For all three flame settings, it is observed that the change in cooling flow control pressure from 0 to 10 psi resulted in mostly internal impingement cooling, which produces an overall temperature reduction but not much change in shape of the temperature profile. The increase in cooling flow control pressure from 10 to 20 psi produces a more obvious air film cooling effect: besides a reduction in temperature, there is a significant change in temperature profile shape where the temperature decrease is much greater just downstream of the leading edge showerhead cooling holes than further downstream. To a lesser extent, this is also observed just downstream (to the left) of the cooling holes in the center of the profile.

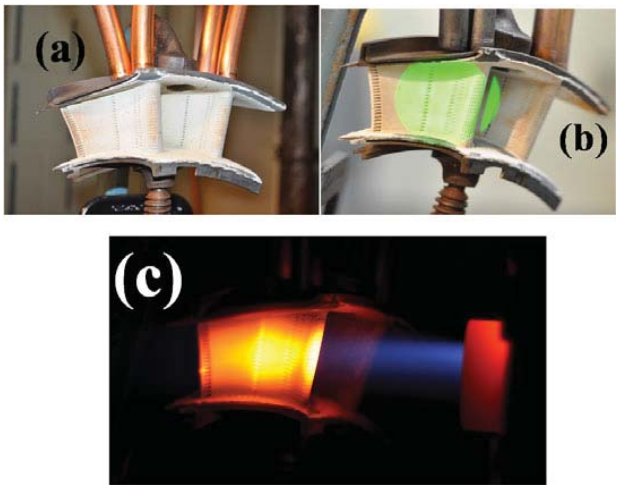

Figure 21.—(a) Photograph of Cr:GAP-coated Honeywell stator vane doublet showing copper tubing used to force air through the vane's cooling hole. (b) Broadened excitation laser beam (532 nm wavelength) illuminating area of interest near leading edge of left-hand vane. (c) Photograph of stator vane doublet positioned in high gas flow flame of NASA GRC Mach 0.3 burner rig facility.

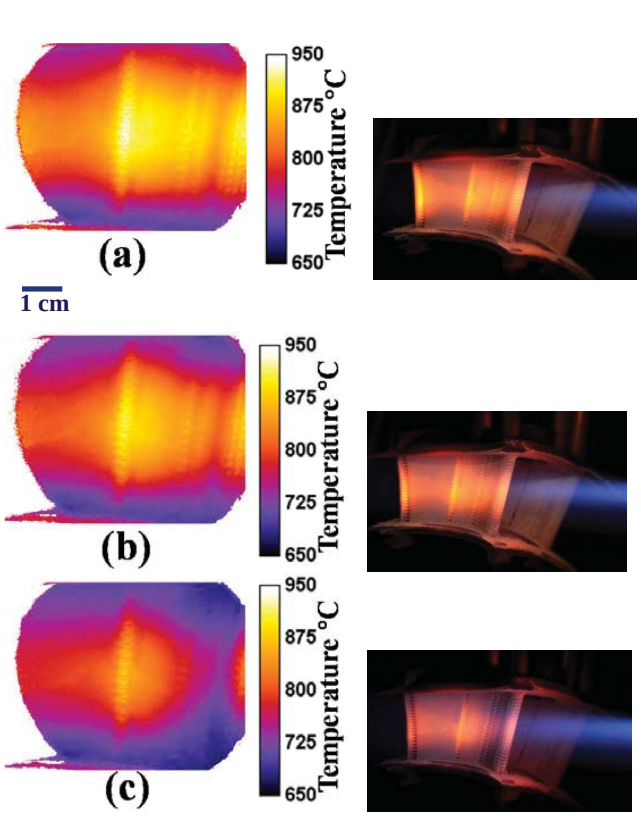

Figure 22.—Surface temperature maps of left-hand vane in burner rig flame at low burner flame setting over range of cooling air flow settings: (a) 0 psi, (b) 10 psi, and (c) 20 psi cooling flow control pressure. Maps produced from 64-gate-delay sequences, 2 on-chip accumulation repeats for each gate delay, gate delay increment = gate width = 7.5 μs. 10 delay sequences averaged. Photographs are of stator vane doublet in burner rig flame at corresponding cooling air flows.

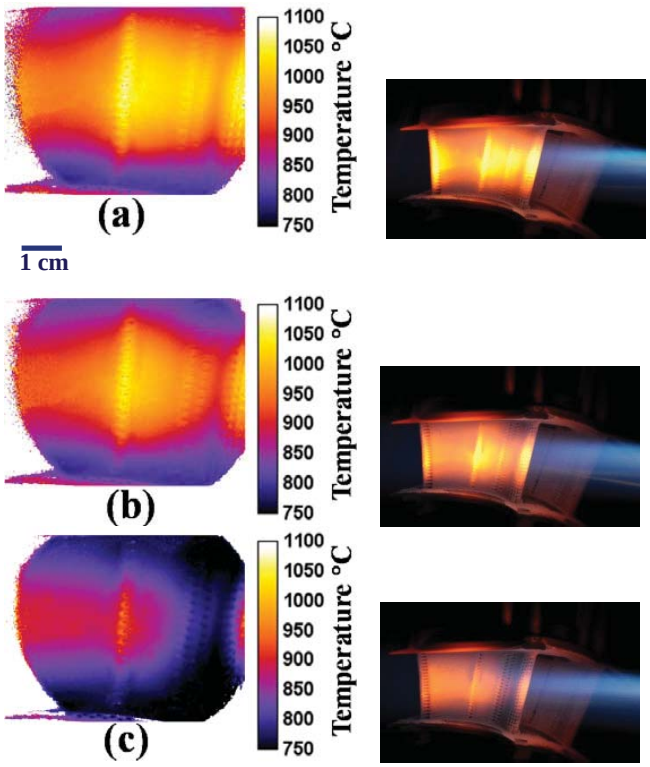

Figure 23.—Surface temperature maps of left-hand vane in burner rig flame at medium burner flame setting over range of cooling air flow settings: (a) 0 psi, (b) 10 psi, and (c) 20 psi cooling flow control pressure. Maps produced from 64-gate-delay sequences. 10 delay sequences averaged. (a) and (b) 8 on-chip accumulation repeats for each gate delay, gate delay increment = gate width = 1.25 μs; (c) 4 on-chip accumulation repeats for each gate delay, gate delay increment = gate width = 2.5 μs. Photographs are of stator vane doublet in burner rig flame at corresponding cooling air flows.

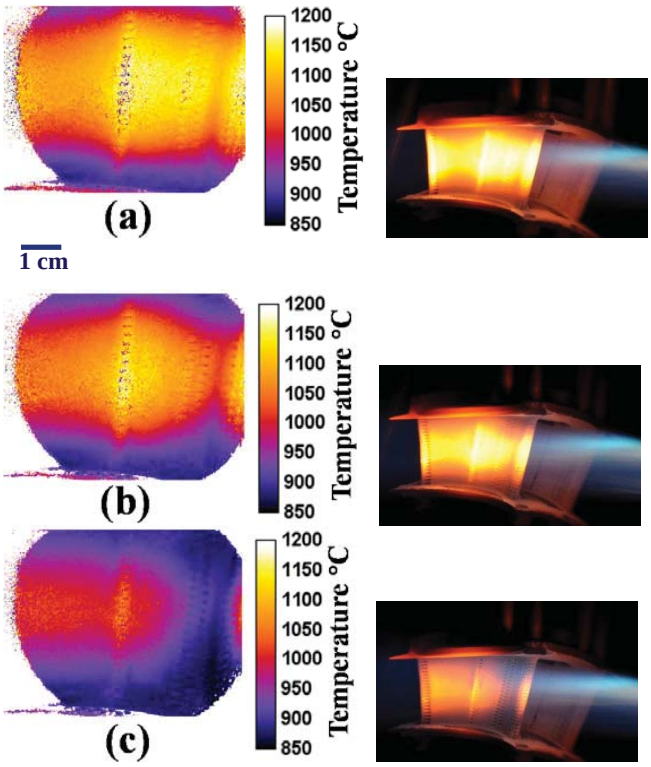

Figure 24.—Surface temperature maps of left-hand vane in burner rig flame at high burner flame setting over range of cooling air flow settings: (a) 0 psi, (b) 10 psi, and (c) 20 psi cooling flow control pressure. Maps produced from 32-gate-delay sequences, 8 on-chip accumulation repeats for each gate delay, gate delay increment = gate width = 0.625 μs. 10 delay sequences averaged. Photographs are of stator vane doublet in burner rig flame at corresponding cooling air flows.

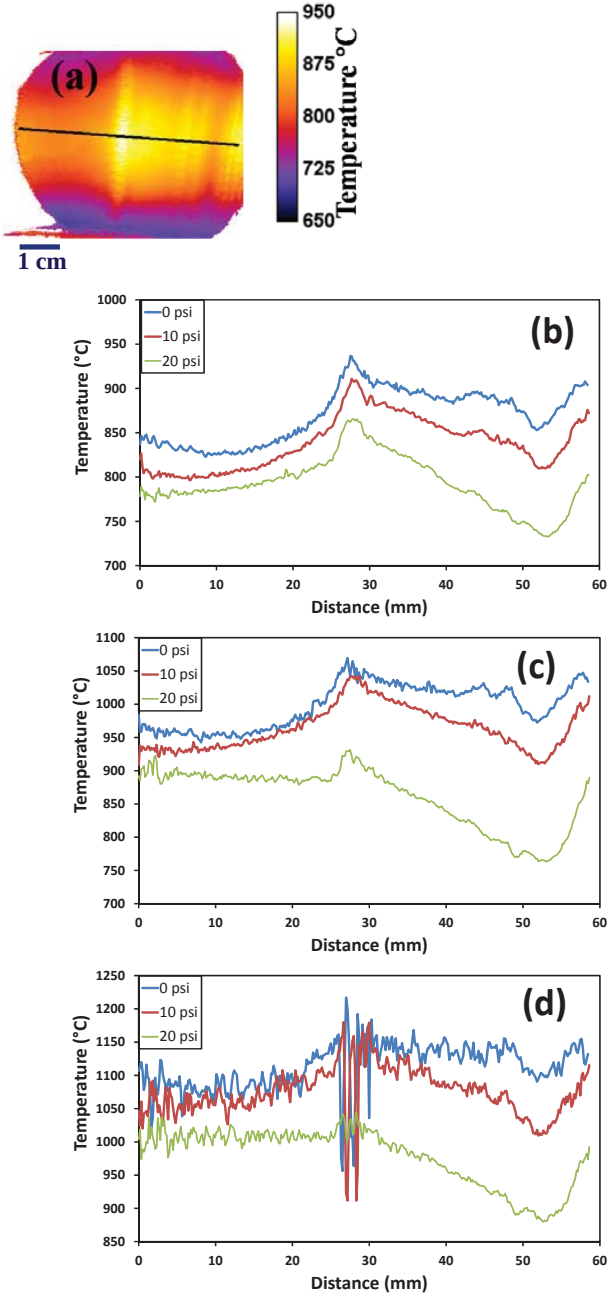

Figure 25.—Temperature line scans across temperature maps of vane in burner flame. (a) Black line indicates location of line scan traversing from left (downstream) to right (upstream) for condition of low burner flame setting and 0 psi cooling flow control pressure. Line scans from other temperature maps shown below are from same location. (b) Temperature line scans at low burner flame setting and three cooling flow levels. (c) Temperature line scans at medium burner flame setting and same three cooling flow levels. (d) Temperature line scans at high burner flame setting and same three cooling flow levels.

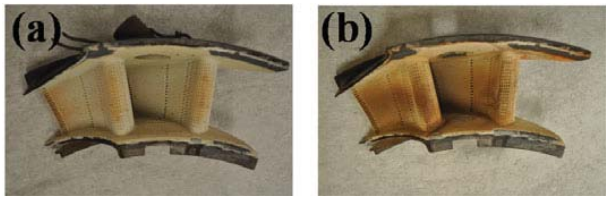

Figure 26.—Photographs of Cr:GAP-coated Honeywell stator vane doublet before (a) and after (b) rust deposition due to burner rig exposure.

It was subsequently discovered that sometimes a significant rust stain was deposited on the vane where it had been exposed to the burner rig flame (Fig. 26). It was concluded that the rust deposit formed when the burner rig had been idle for an extended period and there had been a build-up of moisture in the steel pipes feeding air to the burner rig. Although the rust deposition was inadvertent, this surface deposition offered the opportunity to investigate the effects of a surface deposit on the temperature measurements. Figure 27 compares surface temperature maps obtained from a clean vane surface with those obtained from the same surface with a rust deposit. These temperature maps were obtained at three flame settings with no cooling air flow. The luminescence-based surface temperature maps acquired from the rust-stained surfaces suffered from the attenuation by the rust deposit that significantly reduces signal to noise of the luminescence emission signal. While it was impressive that temperature maps could be obtained through the rust stain, the greatly increased scatter as well as an offset in temperature shows that it is inadvisable to use the luminescence-based temperature mapping in conditions where surface deposits occur. To ascertain whether the loss of signal due to surface degradation was irreversible, a procedure was developed to remove the rust deposit by a combination of applying the cleaning product Bar Keepers Friend (SerVaas Laboratories, Indianapolis, IN) (available at Walmart and other fine establishments) followed by a light grit blasting. It was determined that luminescence emission intensity was recovered with this cleaning procedure.

Surface Temperature Measurements of Vane in Engine Afterburner Flame

While the NASA GRC Mach 0.3 burner rig provided an excellent test bed for developing surface temperature mapping of a component surface, the burner flame produces localized heating that is not representative of the more uniform heat flux present inside a turbine engine. To investigate the more relevant effects of air film cooling in a uniform heat flux with high gas flow velocity, the culminating test of the Phase II effort was temperature mapping in the afterburner flame of a J85 turbojet test engine at UTSI operated by AEDC. The afterburner flame environment of the J85 test engine provides a much more uniform, stable heat flux over the dimensions of the stator vane doublet and produces gas velocities approaching Mach 1 that are closer to a turbine engine environment. The AEDC-designed vane mount supplied cooling air flow through the vane cooling holes. Figure 28 shows the stator vane mounted just aft of the afterburner, with the laser, ICCD, and the 8-μm pyrometer all aimed at the same vane location.

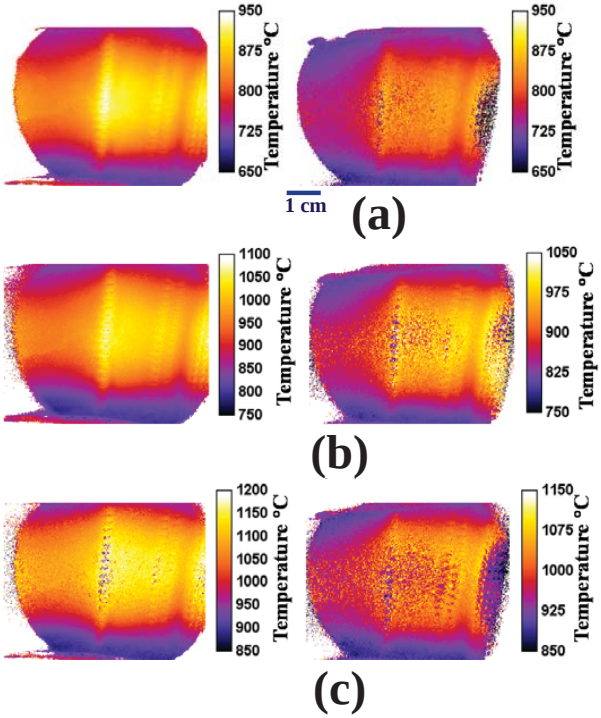

Figure 27.—Comparison of surface temperature maps of left-hand vane in burner rig flame without (left) and with (right) rust stain deposit on vane surface. No cooling air flow. (a) low, (b) middle, and (c) high burner flame setting.

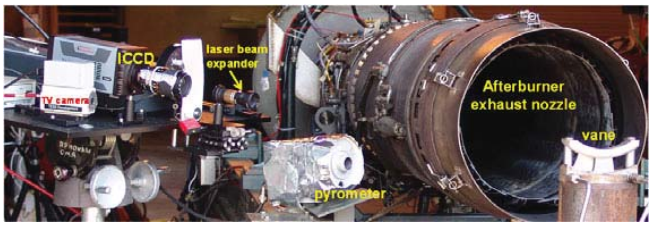

Figure 28.—Photographs of Cr:GAP-coated Honeywell stator vane doublet positioned aft of the J85 engine afterburner exhaust nozzle. ICCD, laser beam expander, and 8-μm pyrometer are aligned to focus on the same region of the vane surface.

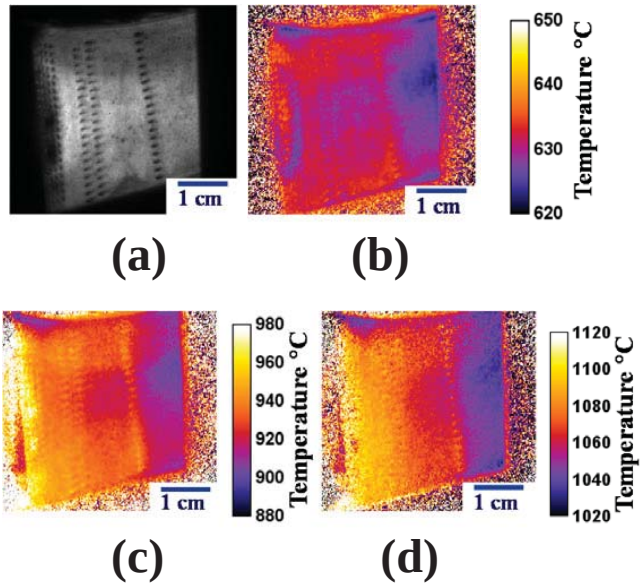

Figure 29.—Surface temperature maps of Honeywell stator vane exposed to afterburner flame of J85 test engine at UTSI with cooling air flow through cooling holes. (a) Field of view for temperature mapping. Temperature maps at different afterburner throttle settings. (b) PLA = 90. Map produced from 64-gate-delay sequences, 10 on-chip accumulation repeats for each gate delay, gate delay increment = gate width = 25 μs. 10 delay sequences averaged. (c) PLA = 99. Map produced from 16-gate-delay sequences, 20 on-chip accumulation repeats for each gate delay, gate delay increment = gate width = 2 μs. 8 delay sequences averaged. (d) PLA = 101. Map produced from 8-gate-delay sequences, 20 on-chip accumulation repeats for each gate delay, gate delay increment = gate width = 1 μs. 8 delay sequences averaged.

Surface temperature maps were obtained at several afterburner throttle positions (Fig. 29). The afterburner throttle positions are indicated by the corresponding power lever angle (PLA). At the highest throttle settings, there are signs of air film cooling as indicated by the discrete temperature reduction observed just downstream from the cooling holes furthest to the right (most downstream). There is also a smaller temperature reduction across the double row of cooling holes closer to the leading edge. This effect of air film cooling, however, was rather modest. The largest cooling effect that was observed was across the holes furthest from the leading edge at the highest throttle setting observed, PLA = 101 (Fig. 29(d)), corresponding to a ΔT of only about 8 °C. While this shows that the surface temperature mapping is impressively sensitive to relatively small temperature differences, it also shows that the test geometry only produced very modest air film cooling.

Low Power Excitation

While a high peak power laser is typically utilized for thermographic phosphor temperature measurements, these lasers are expensive and too massive to be considered for on-wing measurements. In comparison, light emitting diodes (LEDs) and laser diodes (LDs) are vastly less expensive and much more compact. Motivated by the feasibility of obtaining adequate signal to noise from low power excitation sources due to the ultra-bright Cr:GAP luminescence intensity, integrating laser diode excitation into a probe designed for engine insertion was carried out by Emerging Measurements and demonstrated at the NASA GRC high heat flux laser facility and Mach 0.3 burner rig. After comparing several laser diode and LED excitation sources, a laser diode that emits 200 mW at 532 nm was downselected. As shown in Figure 30, this small laser diode was coupled into the fiber injection leg of the engine probe. Integration of the laser diode with the engine probe was pursued because the engine probe can only sample a small solid angle of luminescence emitted from the specimen surface and therefore would serve as a good evaluation of whether adequate signal to noise could be achieved with the low power laser diode excitation source in a practical situation. Figure 31 shows the sensing end of the engine probe positioned above the specimen mounting stage of the high heat flux laser rig. Figure 32 shows luminescence decay curves acquired through the engine probe using low power laser diode excitation, showing excellent signal to noise in the 500 to 700 °C range. Adequate signal to noise for temperature measurements was achieved up to 900 °C. Above 900 °C, it was discovered that laser diode excitation meets a fundamental obstacle. The obstacle to higher temperature use of low power excitation is that low power excitation relies on pulse duration to make up for lower intensity. However, the build-up of luminescence emission with longer pulse widths is limited by the decay of the emission. Atakan et al. (Ref. 20) have pointed out that the luminescence intensity dependence on excitation pulse length can be estimated by:

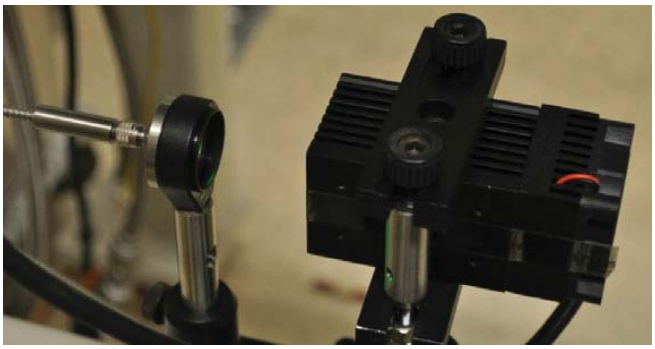

Figure 30.—Compact 532 nm laser diode positioned to couple into excitation fiber optic leg of engine probe.

$$I(t_{pl}) = I_{\max}\left(1 - e^{-\frac{t_{pl}}{\tau}}\right) \tag{3}$$

where $I(t_{pl})$ is the luminescence intensity for a given pulse length, t_{pl}, $I_{\max}$ is the maximum possible luminescence intensity (at $t_{pl} = \infty$), and τ is the phosphor decay time. If an optimum pulse length is selected on the basis of giving a luminescence

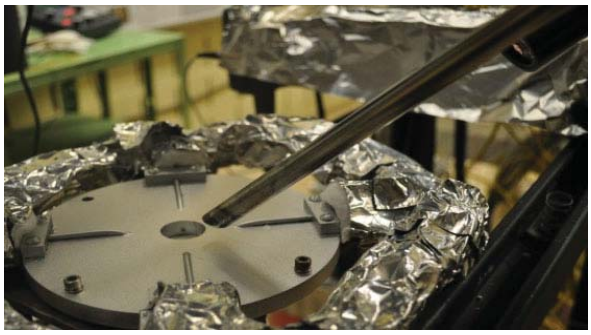

Figure 31.—Sensing end of engine probe positioned above high heat flux laser facility mounting stage.

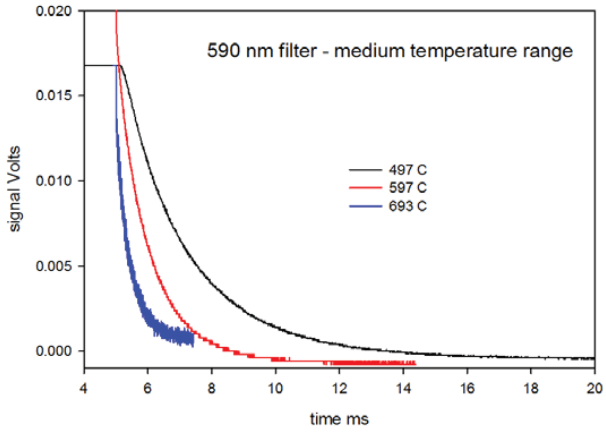

Figure 32.—Luminescence decay curves obtained from 500 to 700 °C from Cr:GAP-coated specimen using low power laser diode.

intensity of 90 percent of I_{max}, then the optimum excitation pulse length will be:

$$t_{pl} = 2.3 \cdot \tau \quad (4)$$

Further increases in excitation pulse length beyond 2.3τ will not produce a significant increase in emission because the intensity is already at 90 percent of I_{max}. At lower temperatures where the phosphor decay times are long, the long optimum excitation pulse widths can be used to build up emission intensity comparable to that from a pulsed laser. For example, at 23 °C, the optimum excitation pulse length is 30 ms ($2.3\times\tau_{23\ °C}$ = 2.3×13 ms), and therefore, the energy delivered by the 200 mW laser diode is 6 mJ, which is comparable with pulsed lasers. However, at 900 °C, the optimum excitation pulse length is only 60 μs ($2.3\times\tau_{900\ °C}$ = 2.3×25 μs), an interval that translates into a mere 12 μJ of laser diode energy, about three orders of magnitude less than a typical pulsed laser. While it was impressive that temperature measurements could be obtained at such low excitation powers up to 900 °C, it was determined that for Cr:GAP, the decay time is too short above 900 °C (decay time at 900 °C = 25 μs) to produce sufficient luminescence emission using the low power laser diode excitation.

Impact Outside of Seedling Project

Honeywell Engine Test

On the basis of the impressive engine probe temperature measurements obtained at UTSI (Figs. 9 and 10), the Air Force decided to adopt Cr:GAP as one of two thermographic phosphors for the Honeywell engine tests that were performed on the Honeywell HTF7000 turbofan engine from a Bombardier business-class turbojet during the week of May 20, 2013 at the Honeywell San Tan Test Facility outside of Phoenix, Arizona. The primary objective of these tests was to demonstrate that reliable thermal barrier coating (TBC) surface temperatures based on luminescence decay of a thermographic phosphor could be obtained from the first high-pressure turbine stage in an operating commercial engine. While the Cr:GAP thermographic phosphor performed better than all other candidate phosphors at NASA and UTSI test facilities, the Cr:GAP phosphor unfortunately went from “first to worst” in actual engine testing. This unsuccessful performance was a consequence of the orders of magnitude higher background thermal radiation encountered in the engine test compared with background levels in any of the combustion test facilities. The background radiation issue is clearly demonstrated in Figure 33, which compares the intense background radiation from the engine (running at full power) exiting the luminescence emission collection fiber bundle with the Cr:GAP luminescence emission collected by the same bundle at room temperature. In Figure 33, the Cr:GAP emission intensity was multiplied by a factor of 10000 in order to be discernible when compared with the background radiation that overwhelmed the luminescence emission. Figure 34 is a photograph of the light exiting the collection fiber bundle leg of the probe observed in an undarkened room, providing a qualitative indication of the overwhelming background radiation intensity. Subsequent discussions with engine company experts made it clear that the objective of measuring temperature of the leading edge of the first stage may have been overly ambitious because of the direct reflection of the combustion environment from this location, and that pyrometer measurements are not even possible at this engine location. Despite this setback, this rare opportunity for installing a probe on an operating engine will be enormously useful for guiding future developments. In particular, these test results have made it apparent that successful temperature measurements of the first stage vane leading edge (where the probe was aimed) or turbine blade will require a phosphor with a much shorter emission wavelength where background radiation would be orders of magnitude lower. This has provided a new direction to research both within and outside NASA to develop a thermographic phosphor with intense ultraviolet wavelength emission.

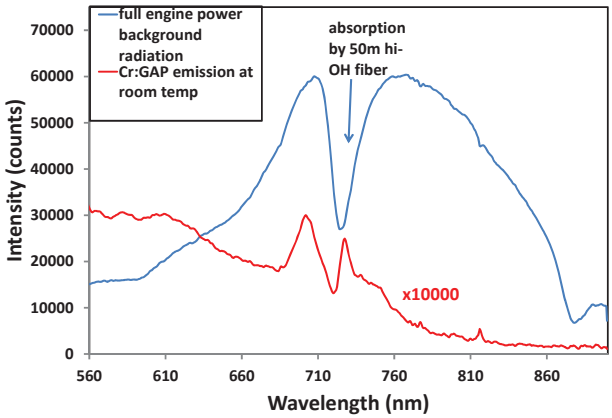

Figure 33.—Spectral plot comparing intensity of the thermal background collected by engine probe at full engine power with luminescence emission intensity collected from Cr:GAP-coated vane surface at room temperature using same engine probe. Note that emission from the Cr:GAP phosphor has been multiplied by a factor of 10000 in order to be discernible.

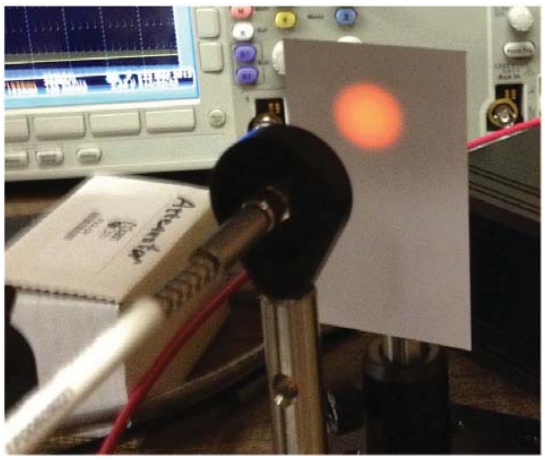

Figure 34.—Intense background engine radiation exiting luminescence emission collection fiber bundle leg of Honeywell engine probe.

Adoption by NASA Projects

The impressive performance of the Cr:GAP phosphor from the testing at NASA and AEDC also led to this phosphor being adopted for temperature measurements from rotating blades on a Pratt & Whitney F117 engine as part of the NASA Vehicle Integrated Propulsion Research (VIPR) project. This rotating blade application will introduce challenges well beyond the scope of the Phase II Seedling effort. However, the turbine blade location will be more favorable for Cr:GAP performance because this location is more shielded from engine radiation than the leading edge of the first stage vane measured in the Honeywell engine. The Cr:GAP phosphor has been successfully deposited by EB-PVD at Penn State onto a turbine blade, has passed a cooling hole air flow inspection test, and has been installed by Pratt & Whitney into its F117 engine along with two blades with other thermographic phosphor coatings. The actual engine test, where the temperature of the rotating blade will be monitored during volcanic ash ingestion, is scheduled for summer 2015.

Temperature mapping using lifetime imaging of Cr:GAP luminescence has also been adopted as an important tool in a more recent ARMD Seedling Phase I award for a combustion group task titled “Real-Time Closed-Loop Modulated Turbine Cooling.” In this project, Cr:GAP thermographic phosphor temperature mapping measurements will monitor effects of adaptive cooling, where cooling flow through cooling holes can be adjusted to provide more effective, uniform cooling. Adaptive cooling will rely on the temperature mapping feedback.

There should be a natural infusion of this technology into the NASA ARMD Aeronautical Sciences Project (currently transitioning to the Transformative Aeronautics Concepts Program), where one of the areas of emphasis in the Innovative Measurements Task is the development of innovative temperature measurements suited for the turbine engine environment.

Summary

The ARMD Seedling Phase II project successfully exploited the retention of ultra-bright luminescence from Cr:GAP at temperatures over 1000 °C, demonstrated in Phase I, to advance the state of the art in engine test facility surface temperature measurement capabilities. These advances include (1) overcoming the limited laser excitation intensity and solid angle of detection necessarily associated with non-intrusive engine probes to achieve reliable spot temperature measurements, (2) transitioning from spot temperature measurements to full-field surface temperature mapping of engine components, and (3) demonstrating temperature measurements using low-powered LED or laser diode excitation integrated into an engine probe.

Reliable spot temperature measurements based on Cr:GAP luminescence decay were successfully demonstrated for a stator vane doublet in the afterburner flame of the J85 test engine at UTSI using a probe designed for engine insertion. The ultra-bright Cr:GAP emission intensity enabled reliable spot temperature measurements over the temperature test range of 500 to 1025 °C despite fiber-limited excitation energy, limited collection solid angle necessary for non-intrusive measurement, and attenuation by surface deposits, factors that combine to reduce signal to noise by orders of magnitude compared with what is possible in the laboratory.

Retention of ultra-bright luminescence intensity above 1000 °C also enabled implementation of full-field surface temperature mapping by broadening the excitation laser beam to cover the area of interest. This approach had not been practical with lower emission intensity rare-earth doped thermographic phosphors because the expansion of the laser

beam reduces excitation energy density, resulting in unacceptably low signal to noise ratio. Surface temperature mapping using Cr:GAP luminescence decay was demonstrated over a range of conditions ranging from well controlled laboratory conditions to more relevant burner rig and engine afterburner environments.

A novel thermal test pattern was developed that was produced by laser heating of Cr:GAP-coated button specimens through a multi-element lens. These thermal test patterns provided well defined thermal patterns for evaluating the temperature sensitivity and spatial resolution of the 2D temperature maps. The acquired 2D temperature maps showed that temperature changes as small as 5 °C over a distance of as little as 0.5 mm could easily be detected, and temperature exceeding 1200 °C could be measured. The thermal test patterns also formed an image database for optimizing the image processing procedures for producing the temperature maps. It was also shown that temperature sampling rates could be increased at the cost of reduced accuracy by substantially reducing the number of gate delays collected.

After demonstrating successful temperature mapping of thermal test patterns, the same approach was applied to more engine-relevant temperature mapping, which included cooling air jet impingement on button specimens, and then advancing to a Cr:GAP-coated stator vane doublet with air film cooling in both NASA burner rig tests as well as UTSI J85 afterburner tests. The effects of cooling air flow were clearly observed in both the burner rig and engine afterburner tests. Temperature maps from burner rig flame exposures showed combined effects of internal impingement cooling and external air film cooling. Temperature maps were obtained with peak temperatures approaching 1200 °C. The temperature maps from the J85 afterburner exposures also showed internal impingement cooling and more modest external air film cooling with peak temperatures of about 1100 °C. In the case of the burner rig tests, an inadvertent surface rust deposit provided an opportunity to investigate the effect of a surface deposit on the temperature mapping. While a temperature map could still be obtained, the resulting signal-to-noise loss and temperature offset result in an unacceptably degraded temperature map.

Successful spot temperature measurements were successfully obtained to 900 °C using a low-power laser diode coupled to an engine probe. Because low power excitation relies on pulse duration to make up for lower intensity to adequately populate the radiating energy state, it was determined that the luminescence decay time for Cr:GAP is too short above 900 °C for low power excitation to be effective at higher temperatures.

Conclusions

Cr:GAP luminescence-decay-based non-intrusive spot temperature measurements as well as full-field temperature mapping of engine component surfaces have been demonstrated for acquiring accurate noncontact surface temperature measurements in engine development facilities. The temperature mapping capability (Figs. 22 to 24 and 29) represents a significant technological advance: the ultra-bright luminescence from the Cr:GAP phosphor provides sufficient luminescence emission from low excitation energy per unit area to produce temperature maps by simply expanding the excitation laser beam to cover the area of interest. Because these luminescence-based temperature measurements are insensitive to surface emissivity and reflected radiation, they can be more reliable for turbine engine environment measurements than thermography or pyrometry. Therefore, it may be beneficial to implement Cr:GAP surface temperature mapping as either a replacement or a calibration reference for temperature maps obtained by thermography or pyrometry. A significant drawback of the luminescence-decay-based temperature mapping was shown to be a susceptibility to substantial mapping degradation when deposits form on the target surface. For this reason, the luminescence-decay-based approach is more suited for engine development facilities and for calibrating thermography or pyrometry measurements than for monitoring temperature throughout long-term engine operating service.

References

1. Allison, S.W. and Gillies, G.T., “Remote Thermometry with Thermographic Phosphors: Instrumentation and Applications,” Rev. Sci. Instrum. 68, 2615-2650 (1997).
2. Brübach, J., Pflitsch, C., Dreizler, A., and Atakan, B., “On Surface Temperature Measurements with Thermographic Phosphors: A Review,” Prog. Energy Combust. Sci., 39, 37-60 (2013).
3. Chambers, M.D. and Clarke, D.R., “Doped Oxides for High-Temperature Luminescence and Lifetime Thermometry,” Annu. Rev. Mater. Res. 39, 325-359 (2009).
4. Khalid, A.H. and Kostantinos, K., “Thermographic Phosphors for High Temperature Measurements: Principles, Current State of the Art and Recent Applications,” Sensors, 8, 5673-5744 (2008).
5. Tobin, K.W., Allison, S.W., Cates, M.R., Capps, G.J., Beshears, D.L., Cyr, M., and Noel, B.W., “High-Temperature Phosphor Thermometry of Rotating Turbine Blades,” AIAA J, 28(8), 1485-1490 (1990).
6. Alururi, A., Bonsett, T., Brewington, A., McPheeters, E., and Wilson, M., “Mapping the Surface Temperature of Ceramic and Superalloy Turbine Engine Components Using Laser-Induced Fluorescence of Thermographic Phosphor,” Optics Lasers Eng., 31, 345-351 (1999).
7. Heyes, A.L., “On the Design of Phosphors for High-Temperature Thermometry,” J. Lumin. 129, 2004-2009 (2009).
8. Aldén, M., Omrane, A., Richter, M., and Särner, G., “Thermographic Phosphors for Thermometry: A Survey of Combustion Applications,” Prog. Energy Combust. Sci., 37, 422-461 (2011).

9. Seyfried, H., Särner, G., Omrane, A., Richter, M., Schmidt, H., and Aldén, M., "Optical Diagnostics for Characterization of a Full-Size Fighter-Jet Afterburner," ASME Turbo Expo 2005, GT2005-69058, 813-819 (2005).
10. Omrane, A., Ossler, F., and Aldén, M., "Temperature Measurements of Combustible and Non-Combustible Surfaces Using Laser Induced Phosphorescence," Exp. Ther. Fluid Sci., 28, 669-676 (2004).
11. Fuhrmann, N., Schneider, M., Ding, C.-P., Brübach, J., and Dreizler, A., "Two-Dimensional Surface Temperature Diagnostics in a Full-Metal Engine Using Thermographic Phosphors," Meas. Sci. Technol., 24, 095203 (2013).
12. Steenbakker, R.J.L., Feist, J.P., Wellman, R.G., and Nicholls, J.R., "Sensor Thermal Barrier Coatings: Remote In Situ Condition Monitoring of EB-PVD Coatings at Elevated Temperatures," J. Eng. Gas Turb. Power, 131, 041301-1 to 041301-9 (2009).
13. Gentleman, M.M. and Clarke, D.R., "Concepts for Luminescence Sensing of Thermal Barrier Coatings," Surf. Coat. Technol., 188-189, 93-100 (2004).
14. Eldridge, J.I., Bencic, T.J., Allison, S.W., and Beshears, D.L., "Depth-Penetrating Temperature Measurements of Thermal Barrier Coatings Incorporating Thermographic Phosphors," J. Therm. Spray Technol., 13(1), 44-50 (2004).
15. Eldridge, J.I. and Chambers, M.D., "Temperature Sensing Above 1000 °C using Cr-Doped $GdAlO_3$ Spin-Allowed Broadband Luminescence," in Temperature: Its Measurement and Control in Science and Industry, Vol. 8, AIP Conf. Proc. 1552, 873-878 (2013).
16. Eldridge, J.I. and Chambers, M.D., Temperature and Pressure Sensors Based on Spin-Allowed Broadband Luminescence of Doped Orthorhombic Perovskite Structures, U.S. Patent 8,695,430, Apr 15, 2014.
17. Zhang, Z., Grattan, K.T.V., and Palmer, A.W., "Temperature Dependence of Fluorescence Lifetimes in Cr^{3+}-Doped Insulating Crystals," Phys. Rev. B, 48, 7772-7778 (1993).
18. Lindén, J., Knappe, C., Richter, M., and Aldén, M., "Limitations of ICCD Detectors and Optimized 2D Phosphor Thermometry," Meas. Sci. Technol., 23(3), 035201 (2012).
19. Wüstner, D., Larsen, A.L., Faergeman, N.J., Brewer, J.R., and Sage, D., "Selective Visualization of Fluorescent Sterols in Caenorhabditis Elegans by Bleach-Rate Based Image Segmentation," Traffic, Published Online: 12 Jan 2010.
20. Atakan, B., Eckert, C., and Pflitsch, C., "Light Emitting Diode Excitation of Cr^{3+}:Al_2O_3 as Thermographic Phosphor: Experiments and Measurement Strategy," Meas. Sci. Technol., 20, 075304 (2009).